Energy Advances

Accepted Manuscript

This article can be cited before page numbers have been issued, to do this please use: C. S. Pathak, D. Aloysius, S. Gupta, S. Mukhopadhyay and E. Edri, *Energy Adv.*, 2024, DOI: 10.1039/D4YA00487F.

ROYAL SOCIETY OF CHEMISTRY

rsc.li/energy-advances

View Article Online
DOI: 10.1039/D4YA00487F

Highly Conductive Flat Grains of Cesium Lead Bromide Perovskite via Additive Engineering with Methylammonium Bromide

Chandra Shakher Pathak[1, 2] *, Deepak Aloysius[3], Satyajit Gupta[3,*], Sabyasachi Mukhopadhyay[4] and Eran Edri[1]

[1]Department of Chemical Engineering, Ben-Gurion University of the Negev Beer Sheva, Israel-8410501
[2]Department of Physics, BMS Institute of Technology and Management, Avalahalli, Bengaluru, India-560064
[3]Department of Chemistry, Indian Institute of Technology Bhilai, Chhattisgarh, India-492015
[4]Department of Physics, SRM University - AP, Andhra Pradesh, India-522240

*To whom correspondence should be addressed: cspathak12@gmail.com, satyajit@iitbhilai.ac.in

View Article Online
DOI: 10.1039/D4YA00487F

Abstract

Perovskite solar cells made of inorganic cesium lead bromide ($CsPbBr_3$) have displayed unusually high open-circuit potentials. Yet, the photovoltage efficiency is still lagging behind that of iodide-based halide perovskites. In this study, a multistep solution spin coating process is used to create $CsPbBr_3$ film. The $CsPbBr_3$ perovskite film consists of flat and rounded grains, and the photocurrent of each grain type is imbalanced. Interestingly, a significant current increase in flat grains was observed by conducting atomic force microscopy (c-AFM) at the nanoscale after the addition of methyl ammonium bromide (MABr) as an additive. The addition of MABr results in good optoelectronic quality of perovskite films with highly conductive grains and provides better charge transport and hence improved power conversion efficiency.

Keywords: perovskite, grains, conductivity, additive, photocurrent

View Article Online
DOI: 10.1039/D4YA00487F

Introduction

Organic-inorganic hybrid perovskite solar cells (PSCs) have made significant advancements in recent years, demonstrating steady growth in their development.[1–4] The main factors that help to improve the performance of PSCs are the composition, interface engineering, and light-harvesting characteristics of the perovskite material.[5–9] Perovskite thin films typically exhibit microstructures characterized by grains and grain boundaries (GBs). The engineering of these films, along with microscopic research, is essential for advancing PSCs.

It has also been demonstrated that surface and GBs modifier additives can enhance PSC performance by affecting the morphology and 'surface trap' passivation. Small molecules [10–15], and potassium halide layers[16,17] were adsorbed at the GBs and surfaces to passivate surface defects, reduce non-radiative losses, increase carrier lifetimes, and enhance the open-circuit voltage (Voc). Polymers were incorporated into the precursor solutions to passivate defects, thereby enhancing the performance and extending the lifetime of PSCs. [18–24]

Perovskite solar cells made of inorganic cesium lead bromide ($CsPbBr_3$) have displayed unusually high open-circuit potentials. The photovoltage efficiency, however, continues to be inferior to that of iodide-based halide perovskites. To improve the performance of $CsPbBr_3$ PSCs, a range of additives and interface materials have been employed.[25–33] Huang *et al*.[34] used cesium acetate (CsAc) and ionic liquid methylammonium acetate (MAAc) to suppress the defects and to prepare the uniform, high-coverage $CsPbBr_3$ film with larger crystalline grains. The additive's improved power conversion efficiency (PCE) is attributable to the favorable morphology, decreased non-radiative recombination, and increased interfacial charge transfer. Furthermore, grains or GBs are crucial to the performance and long-term stability of PSCs. For the case of $CsPbBr_3$ the flat grains were normally observed [28,35–41] but the electronic properties of these flat grains have not been

View Article Online
DOI: 10.1039/D4YA00487F

investigated in detail, and their impact on device performance is currently lacking. Earlier we studied the comparison between $CsPbBr_3$ and $MaAPbBr_3$ perovskite and showed that the former perovskite has higher thermal stability[42]. High-resolution studies utilizing electrical modes of scanning probe microscopy (SPM) techniques, such as conductive atomic force microscopy (c-AFM) and Kelvin probe force microscopy (KPFM), can effectively investigate the crucial role of grains and GBs in influencing the performance and stability of PSCs.[7,43–51] Earlier, the factor of 10 current increase caused by thermal aging in the absorbing $CsPbBr_3$ halide perovskite layer was measured using c-AFM.[35]

Using KPFM, one may image the contact potential difference of a material and gain important information at the grains and GBs.[7,43–47,52–55]. KPFM was also employed to demonstrate the shift in the Fermi level of CsPbBr3 with BiBr3 as an additive, which facilitates the efficient separation and transport of photogenerated charge carriers, thereby enhancing device performance.[56]

In this study, we used c-AFM and KPFM to investigate the optoelectronic properties of flat grains with the addition of methylammonium bromide (MABr) to cesium bromide (CsBr) solution as an additive for $CsPbBr_3$ -PSCs. By doping MABr in a CsBr/methanol solution, a high-quality $CsPbBr_3$ perovskite absorber layer is produced, which has a better crystalline quality and a greater photocurrent. The addition of MABr makes the $CsPbBr_3$ grains more conductive especially the flat grains than the bare ones, and a highly significant increase in overall current is observed. We also observed a higher surface potential for flat grains by KPFM measurements, and the optoelectronic quality greatly improved. The overall increase in current was further confirmed by macroscopic measurements of PSCs. We successfully fabricate high optoelectronic quality $CsPbBr_3$ grains and thus perovskite films prepared with optimized MABr having improved morphology, light absorbance, and suitable energy levels for efficient charge transport.

View Article Online
DOI: 10.1039/D4YA00487F

Experimental section

Materials:

Lead bromide (PbBr2, 98+%, extra pure) was purchased from Acros Organics. Cesium bromide (CsBr, 99.9%, metal basis) and bis(trifluoromethane) sulfonamide lithium salt (LiTFSI, 98.0+%) were purchased from Alfa Aesar. Titanium tetrachloride ($TiCl_4$, 99.0%) solution was purchased from Sigma Aldrich, and titanium dioxide (30NR-D TiO_2) paste was purchased from Greatcell Solar Materials. Dimethyl formamide (DMF, 99.0%), acetonitrile (99.5+%), and chlorobenzene (99.9%) were used as purchased from Alfa Aesar. Dimethyl sulfoxide (DMSO, 99.8%) was purchased from Acros Organics. Ethanol absolute (dehydrated, AR CAS 64-17-5), hydrochloric acid, AR 32% (CAS 7464-01-0), and methanol were purchased from Bio-Lab Ltd., Jerusalem, Israel. Isopropanol and 4-tert-butylpyridine (tBP, 96.0%) were purchased from Sigma-Aldrich. PTAA (batch no. 20210512) was purchased from Broun New Material Technology Ltd.

Film and PSCs fabrication.

Alconox detergent powder, deionized (DI) water, acetone, and 2-propanol were used to clean fluorine-doped tin oxide (FTO) substrates for 30 minutes each, followed by 30 minutes of UV-ozone treatment.

Electron transport layer: For deposition of the TiO_2 compact layer, 219 µl of $TiCl_4$ solution was mixed into 1 ml of DI water and stirred until a transparent solution was obtained. The solution was spin-coated on an FTO substrate at 4000 rpm and 2000 rpm/s acceleration for 30 sec, followed by annealing at 450 °C for 30 min in air. A mesoporous TiO_2 (*m*-TiO_2) layer was deposited using a 150 mg ml^{-1} solution of TiO_2 paste in ethanol spin-coated on the compact layer at 4000 rpm and

View Article Online
DOI: 10.1039/D4YA00487F

2000 rpm/s acceleration for 10 sec, followed by annealing at 125, 325, 375, and 450 ℃ for 10, 5, and 30 min, respectively, in air.

Two-step deposition of perovskite film: 1 M of $PbBr_2$ in 1 ml of DMF was stirred at 75 °C for 5 hours, and the solution was filtered with a polyvinylidene fluoride (PVDF) filter with a pore size of 0.45 microns before deposition. The prepared $PbBr_2$ solution was spin-coated on a preheated mesoporous TiO_2 substrate at a speed of 2000 rpm for 30 seconds and annealed at 75 °C for one hour. 0.07 M of CsBr in 1 ml of methanol stirred at 55 °C for 6 hours, and MABr added CsBr stirred at 55 °C for 1 hour. To create a homogenous and dense $CsPbBr_3$ perovskite layer, the solution was spin-coated on a $PbBr_2$ substrate at a speed of 2000 rpm for 30 seconds, annealed at 250 °C for 5 minutes, and the process was repeated five times. Finally, the perovskite film was rinsed with IPA at 2000 rpm for 30 seconds and annealed at 250 °C for 5 minutes. All fabrication processes were done in a normal laboratory environment.

Hole transport layer and top electrode: 12 mg of PTAA in 1 ml of chlorobenzene mixed with 7.5µL of tBP and 7.5µL of LiTFSI (170 mg/ml) was spin-coated 5s at 500 rpm followed by 40s at 2000 rpm. The samples were left overnight in an N_2 environment. Au was thermally evaporated up to 80 nm at $1x10^{-6}$ Torr on the top of the PTAA layer.

Perovskite film characterization XRD measurements were performed using PANalytical's Empyrean multi-purpose diffractometer and a Bruker D8 Advanced XRD machine, both employing a copper K-α source in Bragg-Brentano geometry. The transmittance and absorbance spectra of the films were recorded using an Agilent Technologies Cary 5000 UV-vis-NIR spectrophotometer. Field-emission scanning electron microscopy (FESEM, FEI Nova Nano SEM450) was used to capture SEM pictures. Photoluminescence (PL) measurements were done with Fluorolog 3 (Horiba) with excitation at 345 nm. c-AFM and KPFM measurements were

View Article Online
DOI: 10.1039/D4YA00487F

performed in a typical laboratory environment utilizing an AFM (Asylum Research, Oxford Instruments) under white light illumination and darkness. The light was guided through the optical system from the top. c-AFM and KPFM measurements were performed using a conducting Pt-coated probe (Micromasch NSC14/Ti-Pt) with a radius of curvature less than 35 nm. XPS measurements were carried out using an X-ray photoelectron spectrometer (ESCALAB 250) in an ultrahigh vacuum (1×10^{-9} bar) with an Al Kα X-ray source and a monochromator.

J-V curves of the PSCs were obtained under simulated AM 1.5 G (100 mW cm^{-2}) illumination, produced by a ScienceTech AAA solar simulator, and measured using an Ossila source-meter unit. The light intensity was calibrated to 100 mW cm^{-2} using a standard silicon reference cell certified by the Newport Corporation.

Chronoamperometric analysis of Perovskite films: The chronoamperometric analysis was performed using a three-electrode electrochemical setup, consisting of a working electrode (where MABr dopped $CsPbBr_3$ perovskite thin film samples coated over FTO is used), reference electrode (Ag/AgCl electrode) and platinum (Pt) wire as counter electrode. In addition, 0.1M Tetrabutylammonium Hexafluorophosphate ($TBAPF_6$) solution in Dichloromethane (DCM) solvent, is used as the supporting electrolyte. The analysis was conducted at 0V applied bias. The thin films are illuminated using a 1.5 AM filter solar stimulator.

Results and discussion

c-AFM experiments of glass/FTO/c-TiO_2/m-TiO_2/perovskite with and without MABr were carried out to examine the impact of MABr incorporation on morphology and electrical characteristics at

View Article Online
DOI: 10.1039/D4YA00487F

the nanoscale. The topography and related current map of perovskite films with MABr are shown in Figure 1 under illumination. The topography image of perovskite films shows that the grains have flat and rounded layered surfaces, and this type of structure is normally observed[28,35–41,57] but the investigation of this type of grain has not been done earlier. To gain insight into the conduction behavior of the flat grains, nanoscale photocurrents were mapped using c-AFM. The current is not uniformly distributed throughout the surface for bare film, preferentially flowing through the flat grain sides; however, with increasing MABr, the current is more uniform, and GBs also show higher currents, as shown in Figure 1. We found the average current for the overall area to be 1.18 pA for bare and 100.4 pA for 15 mg MABr film at 0 V, which represents that we significantly enhanced the current. Bias application further enhanced the effective separation of photogenerated charge carriers and increased the photocurrents. The addition of MABr significantly improves the overall current signal's homogeneity, which denotes a stronger electrical conductivity of the film and, thus, improved charge transfer. This shows that the surface trap states were effectively passivated by the MABr. It is worth noting that the GBs exhibit a comparatively larger current flow, which is consistent with more effective charge transfer. For bare film, the grains are inefficient for charge transfer, which results in poor conductivity of the film. Charge transport across the GBs is made more effective by MABr passivation, which lowers the number of non-radiative recombination sites. Accordingly, MABr can enhance the perovskite layer's crystallinity and reduce defects at GBs, which facilitates the charge transfer.

A very low current signal was seen in the flat grains of bare perovskite, indicating poor mobility and/or depleted charge carriers in the flat region. [58]

View Article Online
DOI: 10.1039/D4YA00487F

The current line profile in Figure S1 indicates that the flat grain exhibits a lower current than the rounded grain for bare perovskite. However, after the addition of MABr, the flat grains display a higher current than the bare perovskite and approach the current value of the rounded grains.

The lower current of flat grains than rounded grains was also observed earlier [35]. According to the literature, the various crystallographic orientations may cause discrepant photoresponse [59]. Here, the MABr addition to the perovskite precursor shows that the flat grains become more conductive and show more photocurrent compared to the bare. This enhancement in current is due to the self-passivation more likely at the flat grains, and this improvement in current is due to the addition of MABr which helps to improve the coverage of thin films and reduces the defects. The improved coverage shown by the reduced oxygen signal in the presence of MABr (as shown in Table S1), which implies less exposure of the underlying meso-TiO_2 layer. Increased current results from improved surface covering because it reduced the effect of underlying layers on the overall electrical characteristics.

To reduce non-radiative recombination—a process in which charge carriers recombine without producing an electrical current—defect passivation is essential. Reduced recombination enhances the overall charge carrier lifetime and, consequently, the conductivity of the perovskite layer. For 15 mg MABr with and without bias, almost all grains have a higher current as compared to other films with increased homogeneity. The color differences at grains in the current mapping show the magnitude of the current values, which can be seen in the color scale.

View Article Online
DOI: 10.1039/D4YA00487F

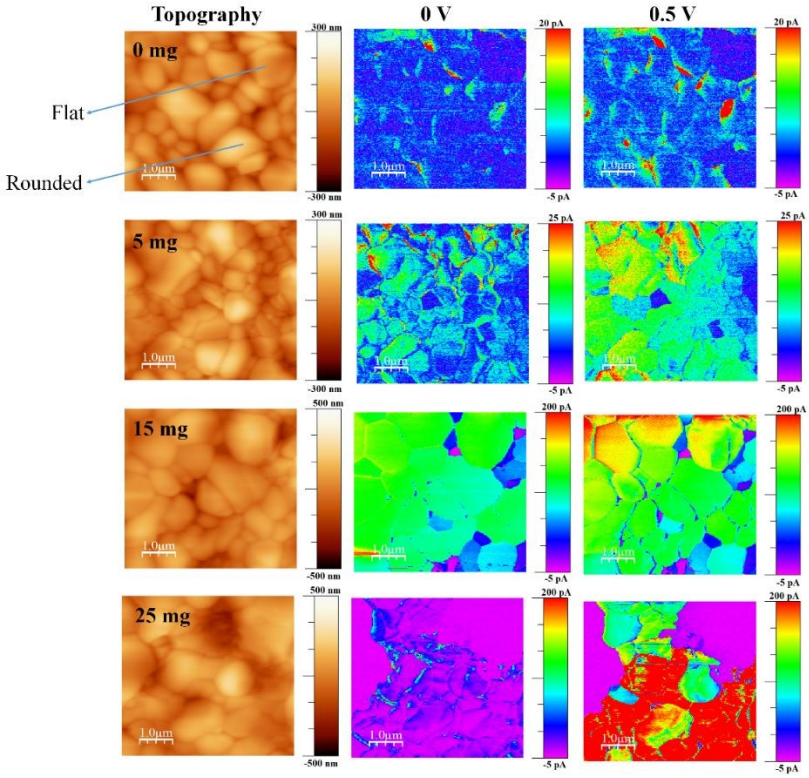

Figure 1. Topography and corresponding current maps of perovskite films with MABr under illumination

There are still a few small low-current areas, which represent the depletion of charge carriers in this area. MABr enhanced the photogenerated electron transport across the whole film. Compared to the others, the local current signal was comparatively more uniform, which implies that the optimal MABr value might coordinate the surrounding perovskite grains and offer a smooth channel for charge transfer in the films. For higher concentrations of MABr, the current is not uniformly distributed; this might be due to the excess amount of MABr, which may induce recombination. Film inhomogeneity and elevated GB photocurrents were previously demonstrated for MAPI, [43,44,53] while smaller GB photocurrents, compared to grain bulk, were shown in fresh triple-cation perovskite films.[47] Also, the chronoamperometric analysis shows a higher

View Article Online
DOI: 10.1039/D4YA00487F

photocurrent response for 15 mg MABr incorporated $CsPbBr_3$ perovskite films in comparison with other films (Figure S3).

The surface potential of the perovskite films was investigated by KPFM. The topography and associated contact potential difference (CPD) maps in the dark and under illumination are shown in Figure 2. Comparing measurements performed in the dark and under illumination shows significant photoresponse and photovoltage. We illuminated the perovskite films from the top, and charge carriers were generated at the perovskite, followed immediately by electron extraction into the electron transport layer (TiO_2) under the built-in electrical field [60] which significantly enhances the overall CPD value under illumination..

We observed the root-mean-square roughness (RMS) of 56.68, 62.66, 90.83, and 114.77 nm for 0 mg, 5 mg, 15 mg, and 25 mg MABr-perovskite films, respectively. For 0 mg, the flat grains show a lower CPD (~40 mV) than the rounded ones, as shown in Figure S4, which implies a deeper Fermi level than the rounder grains and a higher work function. This shows that an upward band bending-induced potential barrier to electron transport may exist at the flat grain. Flat grains with lower CPD are rarely active in the PSCs[61]. Upon addition of MABr flat grains, the CPD shows a slightly higher value (~15 mV) as shown in Figure S4, which is advantageous for increasing the open circuit voltage of devices and is consistent with the results of the *J-V* measurement as shown in Table S2. The CPD line profile in Figure S4 shows that the bare grain has a large variation in CPD, while the 15 mg MABr grain shows almost no change in CPD variations. This suggests that the grain quality is greatly improved with the MABr additive, which is well consistent with the c-AFM results as shown in Figure 1, where the flat grains have a higher current.

The lowest CPD value is shown by 0 mg film, indicating that the bare film has a substantially higher work function than other films. Perovskite films' CPD values dramatically increased after

View Article Online
DOI: 10.1039/D4YA00487F

MABr addition, which implies that the films' work function values were reduced. The enhanced surface potential leads to efficient charge collection probability and suppression of charge recombination. This is also advantageous for increasing the electron transfer efficiency at the interface between perovskite and the electron transport layer.[62] By deducting the CPD value at light from the CPD value at dark, we were also able to measure the photovoltage, and we obtained a photovoltage of 176.4 mV for bare and 418.13 mV for 15 mg MABr-perovskite films. This result is in qualitative agreement with the macroscopic *J-V* results as shown in Table S1, where the 15 mg device has a higher *Voc* than bare. The overall CPD value increase with MABr addition revealed that the MABr modified films lead to self-passivation and optimized charge carrier transport behavior for MABr modified films compared with the bare film. [63,64] The variation in the work function of the sample local surface is reflected in the change in the measured CPD value. [65] We observed a CPD of 650 mV for bare and 926 mV for 15 mg MABr added $CSPbBr_3$ perovskite at dark, which represents the lower work function for MABr perovskite by 0.276 eV. Lower work function means the valence band of MABr-perovskite moves from 5.60 eV to 5.32 eV close to the hole transport layer (HTL) poly[bis(4-phenyl)(2,4,6-trimethylphenyl)amine (PTAA), as shown in supplementary information (Figure S5) [25,56] which facilitate the hole transport to the PTAA and improves the device's performance and decreases surface recombination. [66] Suppressing non-radiative recombination and extending the lifespan of charge carriers depend on defect passivation. Overall perovskite layer conductivity is improved by reduced recombination. The energy levels and band alignment of the $CsPbBr_3$ perovskite can be affected by the addition of MABr. This may cause the valence band edge to move. Changes in the valence band edge can have an impact on how energy levels match with nearby charge transport layers, which can lead to better charge injection and extraction and eventually greater conductivity.

View Article Online
DOI: 10.1039/D4YA00487F

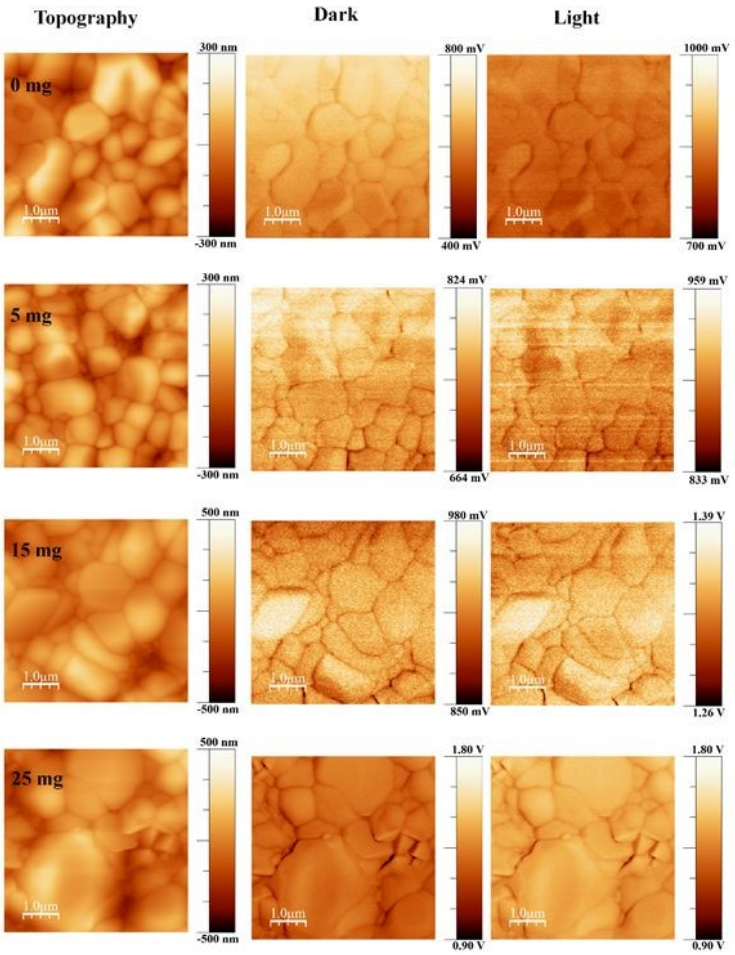

Figure 2. Topography and corresponding CPD maps of perovskite films with MABr under illumination

Scanning electron microscopy (SEM) was used to examine the effect of the MABr additive on the morphology of the perovskite layer, as shown in Figure 3. Bare perovskite films show fewer pin holes, whereas the MABr addition forms uniform and compact films. The grain sizes estimated from SEM images were 580 ±53 nm, 489 ±38 nm, 831±65 nm, and 763 ±33nm for bare, 5, 15, and 25 mg MABr-perovskite films, respectively. We obtained a higher average grain size for the $CsPbBr_3$ film with 15 mg MABr, resulting in fewer grain boundaries. This is advantageous for obtaining a greater open circuit voltage and short circuit current, which supports our findings in Table S2. After MABr addition, the grain size increased slightly, and the ion exchange results in

View Article Online
DOI: 10.1039/D4YA00487F

the final $CsPbBr_3$ product with MABr being supposed to be $MA_xCs_{1-x}PbBr_3$ where x is 0.16, 0.47, 0.78 for 5 mg, 15 mg, 25 mg MABr respectively which is following the shift in peak position from XRD data (Figure 4). Zhu *et al.*[57] also obtained a flat grain structure. They present a mixed-bromide halide exchange technique that eliminates the need for low-solubility CsBr by converting the $CsPbIBr_2$ intermediate phase into $CsPbBr_3$ following spin-coating of MABr/CsBr methanol solution.

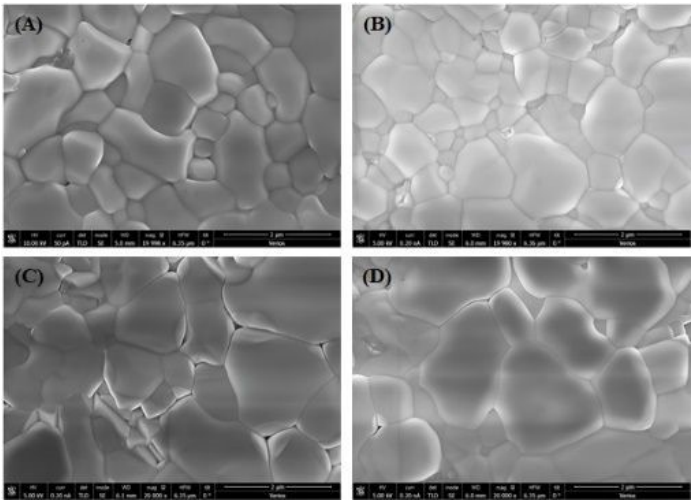

Figure 3. Scanning electron microscopy images of perovskite films with different concentrations of MABr (A) 0 mg, (B) 5 mg, (C) 15 mg, and (D) 25 mg, respectively

X-ray diffraction (XRD) was performed on the perovskite samples with and without the MABr additive. The XRD pattern of $CsPbBr_3$ perovskite shown in Figure 4 with characteristic peaks at 15.20°, 20.7°, 24.1°, 30.7°, 34.5°, and 43.8° corresponds to (100), (110), (111), (200), (210), and (220) planes of cubic $CsPbBr_3$, respectively.[36,67] We found that there is a shift in peak with MABr towards a lower angle compared to the bare film, as a partial replacement of Cs^+ with larger MA^+, which represents the lattice expansion. It suggests that MA^+ cations are incorporated into the perovskite crystal [33] forming an intermediate phase[68] which could be ascribed to the formation of an alloy phase of $MA_xCs_{1-x}PbBr_3$ where x is 0.16, 0.47, 0.78 for 5 mg, 15 mg, 25 mg MABr respectively. The diffraction peaks at 26.4° and 37.8° represent FTO, and the peak at 11.6° was

View Article Online
DOI: 10.1039/D4YA00487F

attributed to the $CsPb_2Br_5$ phase. [38] It represents the excess amount of $PbBr_2$ in perovskite film, and this is generally observed for the two-step deposition process of $CsPbBr_3$ perovskite film, as reported earlier. [69,70] The $CsPb_2Br_5$ phase is suppressed with the addition of MABr until 15 mg, and after that, it again rises.

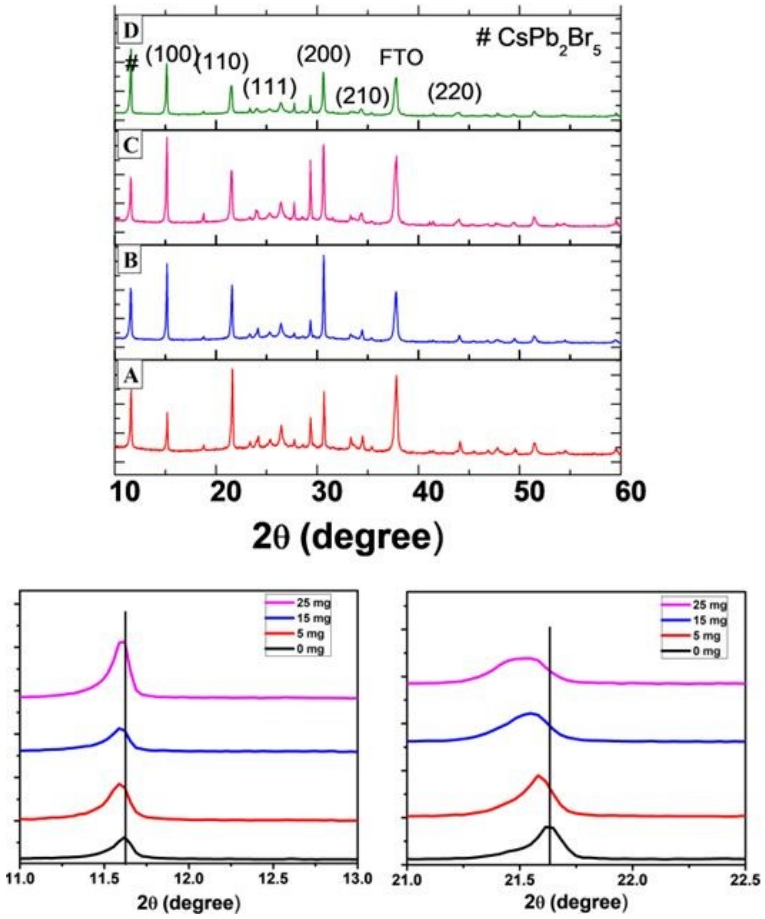

Figure 4. X-ray diffraction patterns of perovskite films with different concentrations of MABr (A) 0 mg, (B) 5 mg, (C) 15 mg, and (D) 25 mg, respectively. The bottom figure gives the zoomed view of the diffraction peak of $CsPb_2Br_5$ and (110) plane

Figures 5 show the absorbance edge of perovskite films and it is almost the same with negligible changes upon MABr addition. Figure 6 shows the PL spectra of $CsPbBr_3$ films with MABr shows

View Article Online
DOI: 10.1039/D4YA00487F

that the PL peak is significantly reduced with 15 mg MABr. This shows that at this doping concentration, the $CsPbBr_3$ light-absorbing layer is more efficient for charge extraction.[23]

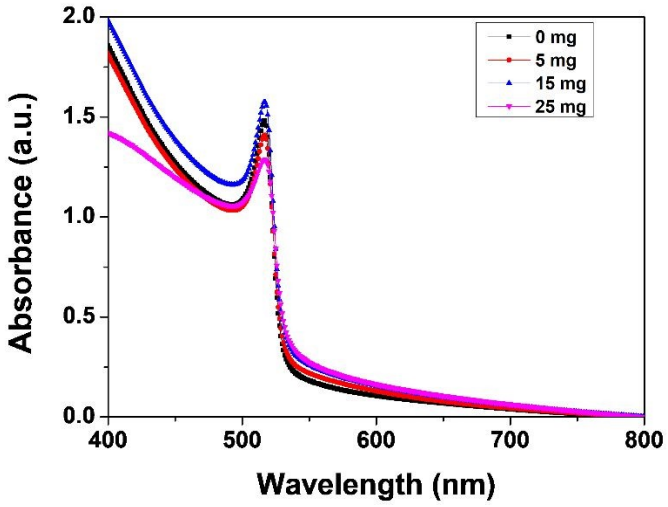

Figure 5: Absorbance spectra of $CsPbBr_3$ with MABr

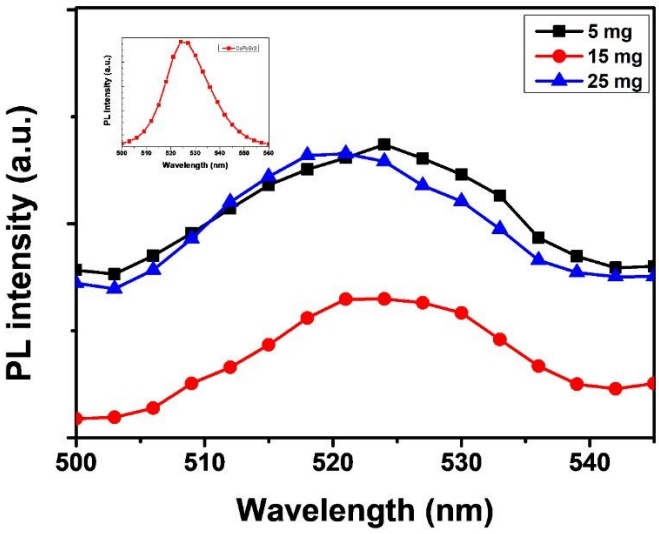

Figure 6: PL spectra of $CsPbBr_3$ with MABr and inset shows the PL spectra of bare perovskite film

View Article Online
DOI: 10.1039/D4YA00487F

To validate the successful doping of MA^+ ions in the perovskite layer, X-ray photoelectron spectroscopy (XPS) was carried out as shown in Figure 7. The N1S spectra demonstrate that MA^+ ions are present in the perovskite layer. From the XPS spectra, a shift was observed in the peak positions of Pb 4f and Br 3d to higher binding energy after the addition of MABr, which is mainly attributed to the redistributed electron density caused by the different binding interaction between the MA^+ ion to Pb and Br. Cs 3d shows obviously less shift. [26,56] The atomic % deduced from XPS is shown in supporting information (Table S1). With the atomic percentages of nitrogen and cesium, one may compute the ratio of MA to Cs. The quantity of nitrogen directly identifies the presence of MA cations because it is specific to MA cations and was absent from the bare perovskite.

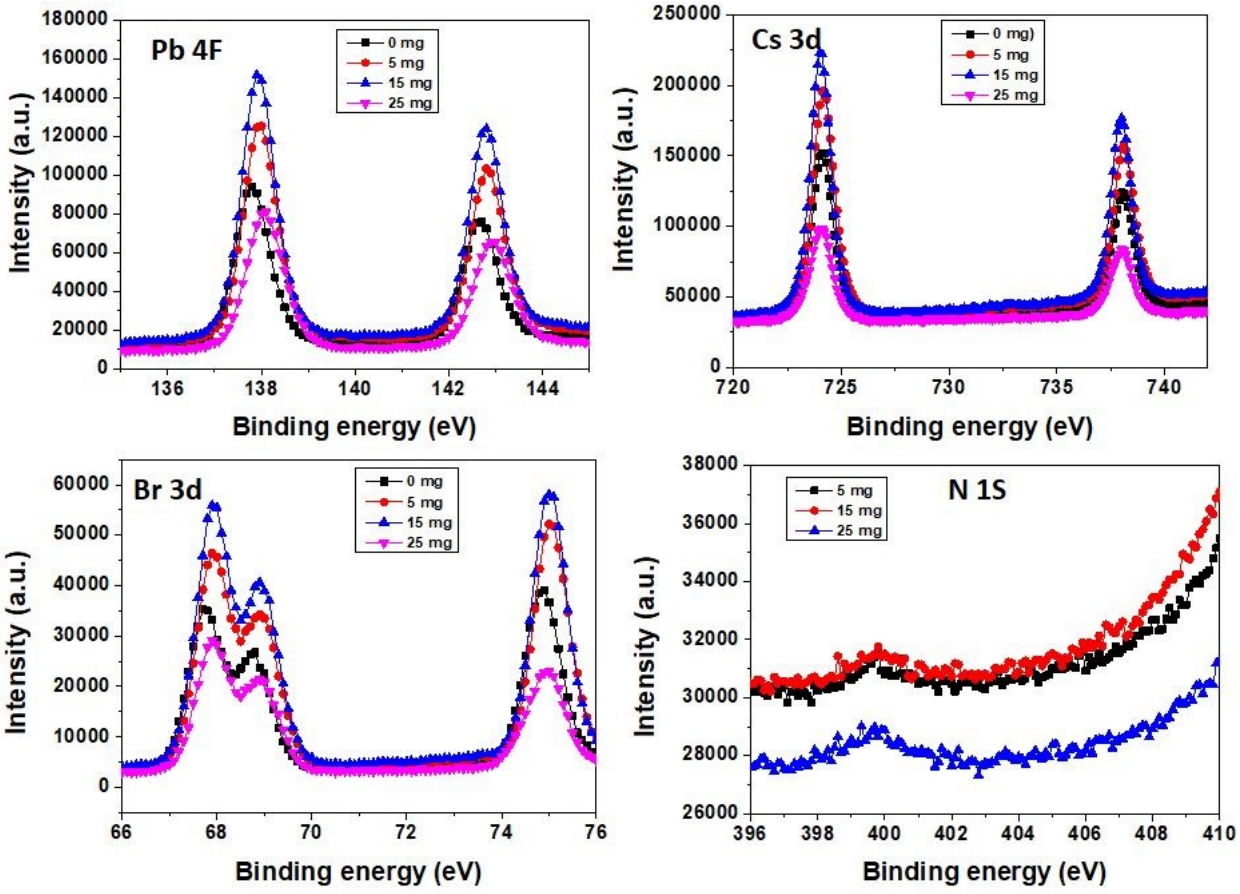

View Article Online
DOI: 10.1039/D4YA00487F

Figure 7. XPS spectra of Pb 4f, Cs 3d, Br 3d and N 1S elements of perovskite films

Under typical 1-sun conditions, the photovoltaic performance was examined using current density-voltage (*J-V*) characteristics. Figure 8 shows the *J-V* characteristics of the best-performing devices with MABr variations. Supporting information (Table S2) shows the average value of photovoltaic performance parameters of glass/FTO/c-TiO_2/m-TiO_2/ perovskite/PTAA/Au solar cells without and with MABr. For the bare film, the grains are inefficient for charge transfer as shown in Figure 1, which results in poor overall performance of the device, while MABr-added devices show enhancements in all device parameters, especially for optimized 15 mg MABr, which can be mainly attributed to the increased conductivity of flat grains, and enhanced carrier transport by MABr. Due to the improved charge carrier transit efficiency as seen in the c-AFM current map (Figure 1), the efficiency of PSCs is improved. The MABr also improves hole transfer to the PTAA, as shown in supporting information (Figure S4), which further explains the improved performance of PSCs with additives. The slight increment in Voc and FF is attributed to the inhibited carrier recombination due to the MABr. J_{sc} enhancement is attributed to the enhanced light harvesting by the $CsPbBr_3$ perovskite layer with MABr addition, which facilitates charge separation and transportation, hence improving Jsc. After an optimal additive of 15 mg MABr, the PCE starts to decrease, which probably indicates the recombination processes and degradation of crystalline quality induced by excess MABr.

View Article Online
DOI: 10.1039/D4YA00487F

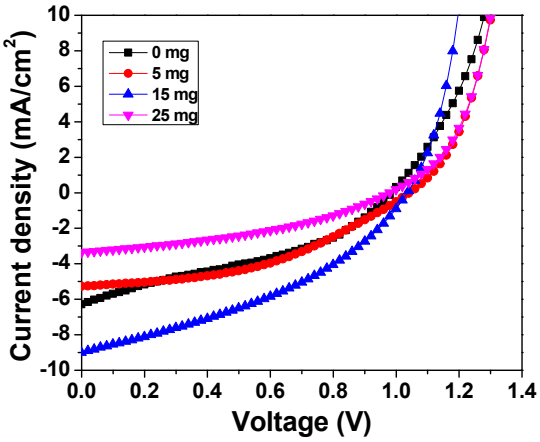

Figure 8. J-V characteristics of $CsPbBr_3$ devices with MABr

Conclusions

Here, our goal was to comprehend how adding MABr affected the electrical characteristics of perovskite grains. We suggest that adding MABr to the precursor solution enhances the conductivity of grains based on results from c-AFM experiments. c-AFM and KPFM measurements show that MABr addition improves the optoelectronic properties of perovskite grains in addition to charge carrier transport and hence increases the PCE. KPFM demonstrated that the valance band of MABr-perovskite moves close to the PTAA, which improves the hole transfer from the perovskite to the PTAA layer.

We demonstrated the benefits of the incorporation of MABr into the CsBr solution to form high optoelectronic quality $CsPbBr_3$ grains. The photovoltaic properties of devices were improved with the addition of MABr to precursor solutions. The present work presents a simple method to enhance the optoelectronic properties of perovskite absorber layers and thus PSCs.

View Article Online
DOI: 10.1039/D4YA00487F

ASSOCIATED CONTENT

Supporting Information

Line section analysis, EDX, chronoamperometric plots, CPD map of perovskite films, energy diagram, and chronoamperometric plots and photovoltaic parameters of devices.

Acknowledgments

We are grateful to Juergen Jopp and Dr. Natalya Froumin for their assistance with SPM and XPS measurements. This research was supported by the Ministry of Science and Technology, Israel, and the Department of Science and Technology, India, through grant number 3-17411. SG and SM acknowledge the DST-India for the Indo-Israeli Joint Research Project (DST/INT/ISR/P-28/2020) for financial support. DA thanks the Ministry of Education for the fellowship.

View Article Online
DOI: 10.1039/D4YA00487F

References

1 T. Miyasaka, A. Kojima, K. Teshima and Y. Shirai, *J. Am. Chem. Soc.*, 2009, **131**, 6050–6051.

2 H. S. Kim, C. R. Lee, J. H. Im, K. B. Lee, T. Moehl, A. Marchioro, S. J. Moon, R. Humphry-Baker, J. H. Yum, J. E. Moser, M. Grätzel and N. G. Park, *Sci. Rep.*, 2012, **2**, 1–7.

3 N. J. Jeon, H. Na, E. H. Jung, T. Y. Yang, Y. G. Lee, G. Kim, H. W. Shin, S. Il Seok, J. Lee and J. Seo, *Nat. Energy*, 2018, **3**, 682–689.

4 J. Park, J. Kim, H.-S. Yun, M. J. Paik, E. Noh, H. J. Mun, M. G. Kim, T. J. Shin and S. Il Seok, *Nature*, 2023, 1–3.

5 T. P. Gujar and M. Thelakkat, *Energy Technol.*, 2016, **4**, 449–457.

6 J. Burschka, N. Pellet, S. J. Moon, R. Humphry-Baker, P. Gao, M. K. Nazeeruddin and M. Grätzel, *Nature*, 2013, **499**, 316–319.

7 Z. Zhao, X. Chen, H. Wu, X. Wu and G. Cao, *Adv. Funct. Mater.*, 2016, **26**, 3048–3058.

8 M. Saliba, T. Matsui, J. Y. Seo, K. Domanski, J. P. Correa-Baena, M. K. Nazeeruddin, S. M. Zakeeruddin, W. Tress, A. Abate, A. Hagfeldt and M. Grätzel, *Energy Environ. Sci.*, 2016, **9**, 1989–1997.

9 T. Singh, M. Ikegami and T. Miyasaka, *ACS Appl. Energy Mater.*, 2018, **1**, 6741–6747.

10 F. Wang, W. Geng, Y. Zhou, H. Fang, C. Tong, M. A. Loi, L. Liu and N. Zhao, *Adv. Mater.*, 2016, **28**, 9986–9992.

11 C. Park, H. Ko, D. H. Sin, K. C. Song and K. Cho, *Adv. Funct. Mater.*, 2017, **27**, 1703546.

12 X. Liu, J. Wu, Q. Guo, Y. Yang, H. Luo, Q. Liu, X. Wang, X. He, M. Huang and Z. Lan, *J. Mater. Chem. A*, 2019, **7**, 11764–11770.

13 C. Lin, J. Lee, J. Kim, T. J. Macdonald, J. Ngiam, B. Xu, M. Daboczi, W. Xu, S. Pont, B. Park, H. Kang, J. Kim, D. J. Payne, K. Lee, J. R. Durrant and M. A. Mclachlan, *Adv. Funct. Mater.*, 2020, **30**, 1906763.

View Article Online
DOI: 10.1039/D4YA00487F

14 C. Lin, F. De Rossi, J. Kim, J. Baker, J. Ngiam, B. Xu, S. Pont, N. Aristidou, S. A. Haque, T. Watson, A. Mclachlan and J. R. Durrant, *J. Mater. Chem. A*, 2019, **7**, 3006–3011.

15 X. Li, J. , M. Ibrahim Dar, Chenyi Yi, M. Tschumi and H. H. and M. G. , Shaik M. Zakeeruddin , Mohammad Khaja Nazeeruddin, *Nat. Chem.*, 2015, **7**, 703–711.

16 M. Abdi-jalebi, Z. Andaji-garmaroudi, S. Cacovich, C. Stavrakas, B. Philippe, E. M. Hutter, A. J. Pearson, S. Lilliu, T. J. Savenije, J. M. Richter, M. Alsari, P. Edward, H. Rensmo, G. Divitini, C. Ducati, R. H. Friend and S. D. Stranks, *Nature*, 2018, **555**, 497.

17 J. Dagar, K. Hirselandt, A. Merdasa, A. Czudek, R. Munir, F. Zu, N. Koch, T. Dittrich and E. L. Unger, *Sol. RRL*, 2019, **3**, 1900088.

18 C. Y. Chang, C. Y. Chu, Y. C. Huang, C. W. Huang, S. Y. Chang, C. A. Chen, C. Y. Chao and W. F. Su, *ACS Appl. Mater. Interfaces*, 2015, **7**, 4955–4961.

19 A. Fakharuddin, M. Seybold, A. Agresti, S. Pescetelli, F. Matteocci, M. I. Haider, S. T. Birkhold, H. Hu, R. Giridharagopal, M. Sultan, I. M. Sero, A. Di Carlo and L. Schmidt-Mende, *ACS Appl. Mater. Interfaces*, 2018, **10**, 42542–42551.

20 D. J. Fairfield, H. Sai, A. Narayanan, J. V. Passarelli, M. Chen, J. Palasz, L. C. Palmer, M. R. Wasielewski and S. I. Stupp, *J. Mater. Chem. A*, 2019, **7**, 1687–1699.

21 D. Wang, L. Zhang, K. Deng, W. Zhang, J. Song, J. Wu and Z. Lan, *Energy Technol.*, 2018, **6**, 2380–2386.

22 C. S. Pathak, G. Paramasivam, F. Mathies, K. Hirselandt, V. S. Der, O. Maus, J. Dagar, C. Klimm, E. Unger and I. Visoly-fisher, *ACS Appl. Energy Mater.*, 2022, **5**, 4085–4095.

23 H. Choi, H. Lim, H. Kim, J. Lim, M. Park, C. S. Pathak and S. Song, *J. Mater. Chem. A*, 2023, **11**, 16363–16369.

24 C. S. Pathak, H. Choi, H. Kim, J. Lim, S. K. Cho, D. S. Ham and S. Song, *Sol. RRL*, 2023, 2300860.

25 H. Guo, Y. Pei, J. Zhang, C. Cai, K. Zhou and Y. Zhu, *J. Mater. Chem. C*, 2019, **7**, 11234–11243.

View Article Online
DOI: 10.1039/D4YA00487F

26 D. Wang, W. Li, Z. Du, G. Li, W. Sun, J. Wu and Z. Lan, *J. Mater. Chem. C*, 2020, **8**, 1649–1655.

27 S. Chen, X. Liu, Z. Wang, W. Li, X. Gu, J. Lin, T. Yang, X. Gao and A. K. K. Kyaw, *Adv. Energy Sustain. Res.*, 2021, **2**, 1–6.

28 D. Wang, W. Li, Z. Du, G. Li, W. Sun, J. Wu and Z. Lan, *ACS Appl. Mater. Interfaces*, 2020, **12**, 10579–10587.

29 Y. Li, J. Duan, H. Yuan, Y. Zhao, B. He and Q. Tang, *Sol. RRL*, 2018, **2**, 1800164.

30 Y. Ren, N. Zhang, Z. Arain, M. Mateen, J. Chen, Y. Sun and Z. Li, *J. Power Sources*, 2020, **475**, 228676.

31 J. Zhu, B. He, Z. Gong, Y. Ding, W. Zhang and X. Li, 2020, 1834–1843.

32 J. Lou, B. Cai, Y. Wu, Y. Lv, X. Liu, W. Zhang and Y. Qin, *J. Alloys Compd.*, 2021, **872**, 159601.

33 Y. X. Zhao Y, Wang Y, Duan J and Tang, *J ournal Mater. Chem. A*, 2019, **7**, 6877–6882.

34 D. Huang, P. Xie, Z. Pan, H. Rao and X. Zhong, *J ournal Mater. Chem. A*, 2019, **7**, 22420–22428.

35 S. Yu, A. F. Akbulatov, L. A. Frolova, S. A. Tsarev, P. A. Troshin and K. J. Stevenson, *Sol. Energy Mater. Sol. Cells*, 2017, **171**, 205–212.

36 X. Liu, X. Tan, Z. Liu, H. Ye, B. Sun, T. Shi, Z. Tang and G. Liao, *Nano Energy*, 2019, **56**, 184–195.

37 W. Zhang, X. Liu, B. He, J. Zhu, X. Li, K. Shen, H. Chen, Y. Duan and Q. Tang, *ACS Appl. Mater. Interfaces*, 2020, **12**, 36092–36101.

38 X. Cao, G. Zhang, L. Jiang, Y. Cai, Y. Gao, W. Yang, X. He, Q. Zeng, G. Xing, Y. Jia and J. Wei, *ACS Appl. Mater. Interfaces*, 2020, **12**, 5325–5931.

39 X. Zhang, Z. Jin, J. Zhang, D. Bai, H. Bian, K. Wang, J. Sun, Q. Wang and S. F. Liu, *ACS Appl. Energy Mater.*, 2018, **10**, 7145–7154.

View Article Online
DOI: 10.1039/D4YA00487F

40 J. Zhu, B. He, Z. Gong, Y. Ding, W. Zhang and X. Li, *ChemSusChem*, 2020, **13**, 1834–1843.

41 X. Li, Y. Tan, H. Lai, S. Li, Y. Chen, S. Li, P. Xu and J. Yang, *ACS Appl. Mater. Interfaces*, 2019, **11**, 23746–29752.

42 M. Kulbak, S. Gupta, N. Kedem, I. Levine, T. Bendikov, G. Hodes and D. Cahen, 2016, 3–8.

43 J. S. Yun, A. Ho-baillie, S. Huang, S. H. Woo, Y. Heo, J. Seidel, F. Huang, Y. Cheng and M. A. Green, *J. Phys. Chem. Lett.*, 2015, **6**, 875–880.

44 J. J. Li, J. Y. Ma, Q. Q. Ge, J. S. Hu, D. Wang and L. J. Wan, *ACS Appl. Mater. Interfaces*, 2015, **7**, 28518–28523.

45 S. Y. Leblebici, L. Leppert, Y. Li, S. E. Reyes-Lillo, S. Wickenburg, E. Wong, J. Lee, M. Melli, D. Ziegler, D. K. Angell, D. F. Ogletree, P. D. Ashby, F. M. Toma, J. B. Neaton, I. D. Sharp and A. Weber-Bargioni, *Nat. Energy*, 2016, **1**, 1–7.

46 J. Xu, A. Buin, A. H. Ip, W. Li, O. Voznyy, R. Comin, M. Yuan, S. Jeon, Z. Ning, J. J. Mcdowell, P. Kanjanaboos, J. Sun, X. Lan, L. N. Quan, D. H. Kim, I. G. Hill, P. Maksymovych and E. H. Sargent, *Nat. Commun.*, 2015, **6**, 1–8.

47 A. Gomez, S. Sanchez, M. Campoy-quiles and A. Abate, *Nano Energy*, 2018, **45**, 94–100.

48 J. Hieulle, C. Stecker, R. Ohmann, L. K. Ono and Y. Qi, *Small Methods*, 2018, **2**, 1–17.

49 Y. Harari, C. S. Pathak and E. Edri, *Nanoscale*, 2023, **15**, 4951–4961.

50 H. Si, S. Zhang, S. Ma, Z. Xiong, A. Kausar, Q. Liao, Z. Zhang, A. Sattar, Z. Kang and Y. Zhang, *Adv. Energy Mater.*, 2020, **10**, 1–23.

51 C. S. Pathak, *Opt. Mater. (Amst).*, 2022, **133**, 113012.

52 C. S. Pathak, B.-J. Chang and S. Song, *Dye. Pigment.*, 2023, **218**, 111469.

53 Y. Kutes, Y. Zhou, J. L. Bosse, J. Steffes, N. P. Padture and B. D. Huey, *Nano Lett.*, 2016, **16**, 3434–3441.

View Article Online
DOI: 10.1039/D4YA00487F

54 J. Yang, X. Liu, Y. Zhang, X. Zheng, X. He, H. Wang, F. Yue, S. Braun, J. Chen, J. Xu, Y. Li and Y. Jin, *Nano Energy*, 2018, **54**, 218–226.

55 Y. Shao, Y. Fang, T. Li, Q. Wang, Q. Dong, Y. Deng, Y. Yuan, H. Wei, M. Wang, A. Gruverman, J. Shield and J. Huang, *Energy Environ. Sci.*, 2016, **9**, 1752–1759.

56 Y. Pei, H. Guo, Z. Hu, J. Zhang and Y. Zhu, *J. Alloys Compd.*, , DOI:10.1016/j.jallcom.2020.155283.

57 W. Zhu, X. Yao, S. Shi, Z. Zhang, Z. Song, P. Gao and T. Wang, *ACS Appl. Energy Mater.*, 2023, **6**, 9798–9804.

58 J. W. Lee, S. H. Bae, Y. T. Hsieh, N. De Marco, M. Wang, P. Sun and Y. Yang, *Chem*, 2017, **3**, 290–302.

59 Y. Wang, Z. Hu, C. Gao, C. Yang, J. Zhang and Y. Zhu, *Adv. Mater. Interfaces*, 2020, **1901521**, 1–8.

60 C. Yang, P. Du, Z. Dai, H. Li, X. Yang and Q. Chen, *ACS Appl. Mater. Interfaces*, 2019, **11**, 14044–14050.

61 A. Dymshits, A. Henning, G. Segev, Y. Rosenwaks and L. Etgar, *Sci. Rep.*, 2015, **5**, 1–6.

62 H. Zeng, L. Li, F. Liu, M. Li, S. Zhang, X. Zheng, L. Luo, S. You, Y. Zhao, R. Guo, Z. Gong, R. Huang, Z. Li, T. Wang and and X. L. Yi Cui, Yaoguang Rong, *Adv. Energy Mater*, 2022, **2102820**, 1–10.

63 A. F. Castro-Méndez, J. Hidalgo and J. P. Correa-Baena, *Adv. Energy Mater.*, 2019, **9**, 1–10.

64 D. S. Lee, J. S. Yun, J. Kim, A. M. Soufiani, S. Chen, Y. Cho, X. Deng, J. Seidel, S. Lim, S. Huang and A. W. Y. Ho-Baillie, *ACS Energy Lett.*, 2018, **3**, 647–654.

65 X. Liu, L. Shi, J. Huang, Z. Liu, P. Zhang, J. S. Yun, A. M. Soufiani, J. Seidel, K. Sun, Z. Hameiri, J. A. Stride, Y. Zhang, M. A. Green, H. Lin and X. Hao, *Sol. RRL*, 2019, **3**, 1–10.

66 L. Zhang, T. Guo, B. Liu, D. Du, S. Xu, H. Zheng, L. Zhu, X. Pan and G. Liu, *ACS Appl.*

View Article Online
DOI: 10.1039/D4YA00487F

Mater. Interfaces, 2022, **14**, 19614–19622.

67 X. Chang, W. Li, L. Zhu, H. Liu, H. Geng, S. Xiang and J. Liu, *ACS Appl. Mater. Interfaces*, 2016, **8**, 33649–33655.

68 J. Zhang, Z. Wang, A. Mishra, J. Zhang, Z. Wang, A. Mishra, M. Yu, M. Shasti, W. Tress, A. Agarwalla, Z. Wang, W. Xiang, L. Emsley and Z. Zhang, *Joule*, 2020, **4**, 222–234.

69 H. Li, G. Tong, T. Chen, H. Zhu, G. Li, Y. Chang, L. Wang and Y. Jiang, *J ournal Mater. Chem. Aournal Mater. Chem. A*, 2018, **6**, 14255–14261.

70 Z. Liu, B. Sun, X. Liu, J. Han, H. Ye, T. Shi, Z. Tang and G. Liao, *Nano-Micro Lett.*, 2018, **10**, 1–13.

- The data supporting this article have been included as part of the Supplementary Information.

View Article Online
DOI: 10.1039/D4YA00487F